Application of a Detached Eddy Simulation Approach with Finite-Rate Chemistry to Mars-Relevant Retropropulsion Operating Environments

Ashley Korzun*, Gabriel Nastac†, Aaron Walden‡, Eric Nielsen§, and William Jones¶
NASA Langley Research Center, Hampton, Virginia, 23681

Patrick Moran‖
NASA Ames Research Center, Moffett Field, California, 94035

Human-scale Mars vehicles will require retropropulsion for descent and landing, replacing heritage supersonic parachute systems with an extended phase of powered flight. Due to the limitations of terrestrial testing in Mars-relevant conditions, design and analysis will increasingly rely on computational modeling and simulation. This paper provides an overview of a computational campaign investigating the aerodynamics of a Mars lander concept along various points on a powered descent trajectory including supersonic, transonic, and subsonic conditions using finite-rate chemistry. Simulations using unstructured grids containing billions of elements are performed at scale using thousands of Graphics Processing Units, enabling run-times of a few days for each simulation presented. At each freestream condition, significant minor species concentrations are observed external to the nozzles in the large mixing region upstream of the vehicle. While the flowfields are highly non-stationary in all cases, the mean integrated forces and moments on the vehicle remain small in comparison to the deceleration provided through retropropulsion.

I. Nomenclature

C_A	axial force coefficient	V	velocity, m/s
C_l	rolling moment coefficient	α	angle of attack, deg
C_m	pitching moment coefficient	β	angle of sideslip, deg
C_N	normal force coefficient	γ	ratio of specific heats
C_n	yawing moment coefficient	μ	mean
c_p	coefficient of pressure	ρ	density, kg/m^3
C_T	thrust force coefficient	σ	standard deviation
C_Y	side force coefficient	τ	time, s
D	diameter, m	0	total condition
M	Mach number	2	post-shock condition
p	pressure, Pa	e	nozzle exit condition
q	dynamic pressure, Pa	j	jet condition
R	radius, m	∞	freestream condition
T	temperature, K		

II. Introduction

RETROPROPULSION in atmospheric flight reemerged as a technology development objective in the mid-2000s, with NASA's primary interest in its application to deceleration and maneuvering to enable entry, descent, and landing

*Aerospace Engineer, AIAA Senior Member.
†Research Scientist, AIAA Member.
‡Research Scientist.
§Senior Research Scientist, AIAA Associate Fellow.
¶Computer Scientist, AIAA Associate Fellow.
‖Computer Scientist.

(EDL) of large payloads at Mars. System performance requirements for human Mars exploration include greater than an order of magnitude increase in payload mass over those deliverable with legacy supersonic parachute technology, and all concepts require supersonic retropropulsion (SRP), or initiation of retropropulsion while the vehicle is traveling at supersonic speeds, as part of an extended powered descent phase of flight [1–3]. Flight-relevant physical scales and Mars-relevant conditions cannot be fully achieved through terrestrial testing, requiring the design and mission infusion of SRP to be heavily reliant on computational modeling and simulation.

Figure 1 shows a simplified SRP flowfield with a single plume, where the supersonic freestream flow approaches from left to right, and the plume flow is from right to left. In the retropropulsion application, the momentum of each flow is comparable, resulting in significant aerodynamic interference. The overall flow obstruction is a combination of the supersonic nozzle exhaust flow structure and the body, or vehicle, both altering the shape and upstream displacement of the bow shock (in the supersonic case). The supersonic nozzle flow extends upstream of the vehicle to meet the opposing supersonic freestream flow, forming a stagnation surface about which the flows slow and are then turned outboard and continue downstream, aft of the vehicle. The overall flowfield is characterized by dynamic, highly non-stationary behavior of most primary flow structures. Significant mixing occurs between the freestream flow and nozzle flows, producing an environment for the vehicle that is no longer composed of primarily local atmosphere. Limitations in ground testing have largely prevented characterization of this mixing and potential impacts of chemistry external to the retropropulsion nozzle(s).

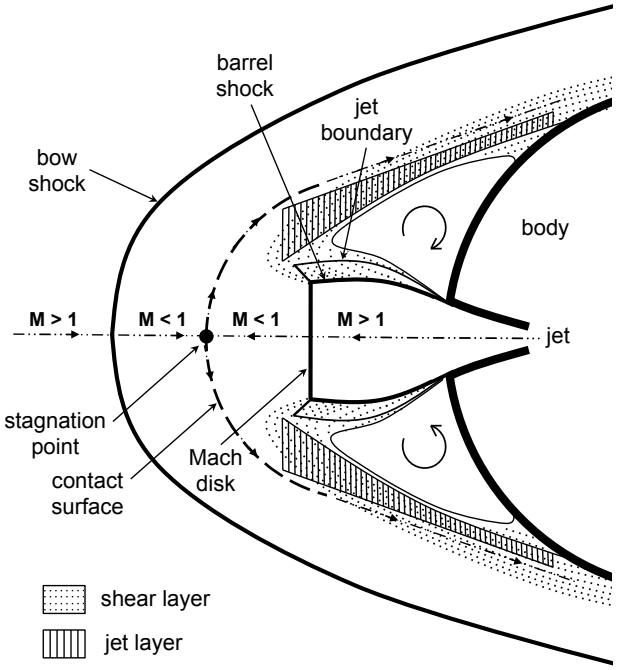

Fig. 1 Simplified SRP flowfield for a single plume (adapted from [4]).

The ability to properly simulate thermodynamic and transport properties of both the Martian atmosphere and the high-enthalpy rocket exhaust is critical to accurate prediction of retropropulsion-induced environments on the vehicle. The obstruction ahead of the vehicle created by retropropulsion governs the magnitude and behavior of aerodynamic variations on the vehicle. As illustrated in Fig. 1, the resulting flowfield structure defining this obstruction is highly dependent on the expansions, shocks, free shear layers, and mixing interfaces comprising it. The conditions, including pressure, temperature, and specific heat capacity, are strong functions of the chemical composition of the local fluid mixture. It is the characterization of this aerodynamic-propulsive interference and uncertainty in dynamic behavior that form the primary challenge for mission infusion of a supersonic powered descent phase of flight [5, 6].

While numerous investigations have been conducted using subscale, inert gas wind tunnel tests as far back as the early 1960s [4], limitations in physical and environmental scaling have led to a renewed emphasis on computational modeling and testing in support of validating such simulations for vehicle-focused quantities of interest. Computational fluid dynamics (CFD) efforts specific to the retropropulsion application have spanned steady and unsteady Reynolds-averaged

Navier-Stokes (RANS) [7–13], detached eddy simulation (DES) [8, 9, 13–20], and large eddy simulation (LES) approaches [21]. RANS and even inviscid [22] methods are generally capable of capturing primary flow features, though the resulting flowfields tend to be much steadier than those observed in experiment due to the RANS models being overly dissipative in capturing highly turbulent free shear layer interactions or damping out the self-excited flow in most scenarios examined. Schauerhamer et al. [8], Kleb et al. [9], and Shafner et al. [17] all observed excessive eddy viscosity production around the wind tunnel model in RANS simulations, preventing turbulent vorticity production in the aerodynamic interference region of the flowfield. As computing power has increased, DES methods have become more prevalent in simulating SRP flows. While DES methods have more accurately captured unsteady behavior and plume structures, there remains some degree of sensitivity to the associated submodel.

Interest in the reusable launch vehicle sector and available flight data have produced opportunities to extrapolate subscale, inert gas experience to much larger flight vehicles and species more representative of real propulsion systems. Frozen and perfect-gas assumptions for two gas mixtures (freestream and retropropulsion exhaust) have been applied with both RANS [10, 16] and LES [16] approaches. NASA CFD simulations, including those using FUN3D, of the SpaceX Falcon 9 first stage during powered booster return flight showed qualitatively good agreement with trends in available flight data for total forces and moments [10]. It must be noted, however, that this vehicle has minimal aerodynamic surface area in the direction of flight and propulsion system performance is dissimilar to the propulsion systems presently specified for Mars exploration, where the systems are more akin to in-space propulsion than first stage launch vehicles. Simulations of Falcon 9 booster return by Ecker et al. [16] from DLR observed significant differences in retropropulsion exhaust gas temperatures between an averaged LES solution and a steady-state RANS solution using a non-reacting mixture of two thermally-perfect gases to represent the freestream and engine exhaust. Such differences in temperature illustrate the limitations of RANS in accurately capturing turbulent mixing in free shear layers and further motivate the application of approaches beyond RANS for SRP flows.

Computational costs of simulating these complex flowfields, where large portions of the computational domain contain largely non-stationary flow features are non-trivial, with costs increasing further as the vehicle scales to flight, DES or LES methods are applied, temporal durations suitable for characterizing unsteady behavior are desired, and real-gas species and chemistry are added. Computing resources have long constrained the simulation of this problem. A prior campaign by the authors [15] utilized a graphics processing unit (GPU)-enabled version of NASA's FUN3D CFD solver to simulate a human-scale Mars lander concept vehicle with retropropulsion. This unique computing capability permitted ensemble simulation of the full-scale vehicle across multiple points along a powered descent trajectory and at different spatial resolution. In all cases, a DES method was applied, and all conditions, both freestream and for the engines, were scaled from flight to perfect-gas air, as required by the GPU-enabled version of the flow solver at the time of this earlier computational campaign.

This paper describes the campaign and results from using a GPU-enabled version of the FUN3D CFD solver to simulate retropropulsion aerodynamics with finite-rate chemistry on a conceptual human-scale Mars lander. This campaign utilizes computational resources and access to the Summit supercomputer provided by the U.S. Department of Energy at Oak Ridge National Laboratory [23]. Section III describes the reference vehicle, computational approach, tools, and run matrix. Section IV discusses results from the campaign, and where applicable, compares results from the present finite-rate chemistry effort with those from the prior, scaled perfect-gas campaign [15], both of which use a DES approach. More comprehensive details on the effect of chemistry for the supersonic condition of this campaign are provided in Ref. [18].

III. Approach, Tools, and Methods

A. Computational Campaign and Geometry

This computational campaign leverages prior exploratory work with RANS CFD [10, 12] and perfect-gas DES efforts [8, 14, 15, 17] to apply a DES approach with finite-rate chemistry to a conceptual, human-scale Mars lander utilizing retropropulsion. Flight-relevant conditions are taken along a nominal powered descent trajectory from Ref. [3, 12], spanning high-supersonic to transonic to high-subsonic speeds. The conceptual vehicle geometry is a low-L/D human-scale Mars lander [3], shown in Fig.2 with a surface habitat as the payload and aft geometry. The heatshield is a 16.4 m diameter 70° sphere-cone, of which the outer part is a Hypersonic Inflatable Aerodynamic Decelerator (HIAD). The eight retropropulsion nozzles for descent and landing are derived from a conceptual liquid oxygen/methane (O_2/CH_4) engine and are assumed to integrate with the lander through the 9.1 m diameter rigid nose of the vehicle.

No scaling of the vehicle geometry or conditions is done for this analysis due to the inclusion of finite-rate chemistry

and flight-relevant composition for both the Martian atmosphere and the engines' equilibrium combustion products. The nozzles, with a nominal exit-to-throat area ratio of 177:1, are canted outboard 5°, and the exit plane of each nozzle is scarfed to have a flush intersection with the heatshield. In this analysis, all eight engines are operating at the same condition (e.g. no differential throttling). Details such as protuberances, doors or cavities housing the engines, the lander deck, and other details of the payload have been neglected in the geometry definition to simplify grid generation and because such design details remain to be defined.

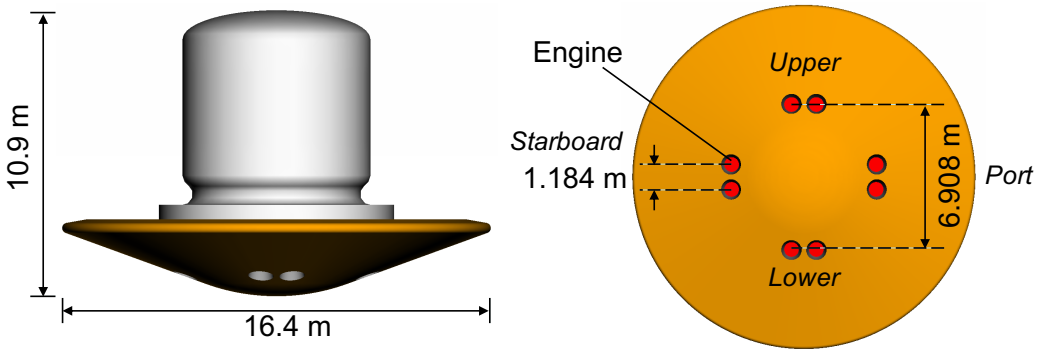

Fig. 2 Vehicle geometry and retropropulsion configuration.

Figure 3 shows the aerodynamics coordinate frame, maintaining the standard convention for entry vehicles, where pitching the nose of the vehicle down produces positive lift. Of note for the vehicle shown in Figs. 2 and 3, there is significant aerodynamic surface area relative to nozzle exit area on the heatshield. The pressure distribution on the heatshield arising from retropropulsion during the descent phase is the focus in this analysis, as the resulting integrated forces and moments on the vehicle created by the aerodynamic-propulsive interference may impact vehicle performance, stability, controllability, and on-board sensor accommodations. For all results presented here, the reference length is the maximum diameter of the vehicle, equal to 16.4 m, and the aerodynamic reference area is the circular area based on the maximum diameter of the heatshield, or 211.24 m^2.

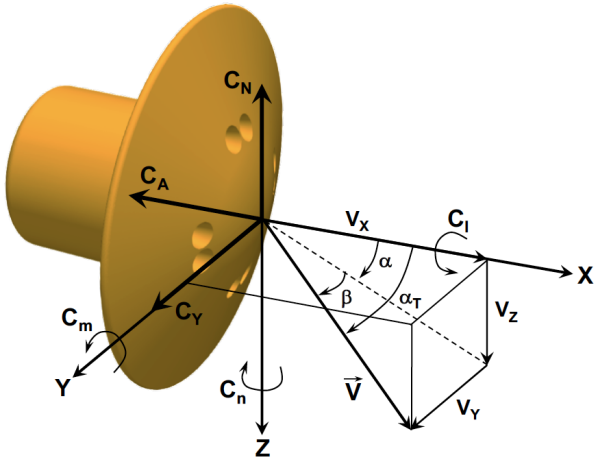

Fig. 3 Aerodynamics coordinate frame (consistent with heatshield view in Fig. 2).

Table 1 provides the freestream conditions for each of the three points along the powered descent trajectory. Flight-time under retropropulsion from Mach 2.4 to Mach 0.8 is approximately 31 seconds. The throttle setting for each engine is held constant at 80% for all three freestream conditions, a realistic assumption given recent performance analyses with guidance and control for this conceptual vehicle [24]. Key similarity parameters are matched between the previous perfect-gas air campaign and the current finite-rate chemistry campaign including: freestream Mach number, Reynolds number, and dynamic pressure, nozzle exit-to-stagnation freestream pressure ratio (matched to the perfect-gas campaign for Mach 2.4 conditions only), and ideal nozzle exit Mach number.

The atmosphere composition is assumed to be 97% CO_2 and 3% N_2 by mass. An equilibrium composition of methane-oxygen combustion products is assumed as the boundary condition for the eight nozzle plena (see Table 3). The total temperature and pressure are approximately 3582 K and 84.46 bar (1224 psi; 8.446×10^6 Pa), respectively, with an oxidizer-to-fuel ratio of 3.5. A 10-species, 19-reaction chemical mechanism is utilized with a one-temperature model. The species included in this mechanism are: CO_2, N_2, C, O, H_2O, H_2, CO, OH, O_2, and H. The set of 19 reactions are shown in Table 2, where M is used to represent a third body.

Table 1 Freestream conditions along a nominal powered descent trajectory.

M_∞	V_∞ (m/s)	T_∞ (K)	p_∞ (Pa)	q_∞ (Pa)	ρ_∞ (kg/m^3)
2.40	560.60	216.53	284.73	1,093.82	0.0070
1.40	329.37	218.63	386.48	507.85	0.0094
0.80	189.10	219.50	442.92	191.16	0.0107

Table 2 Chemical mechanism used for this analysis. Units are in seconds, moles, cubic centimeters, calories, and Kelvin. [a]Rate coefficients are given in the form $k = AT^n e^{-T_a/T}$.

#	Reaction[a]	A	n	T_a	Factors and Reference
1	$CO + M \longleftrightarrow C + O + M$	1.2×10^{21}	−1.0	1.29×10^5	H, O = 1.5, [25]
2	$CO + O \longleftrightarrow O_2 + C$	3.9×10^{13}	−0.18	6.92×10^4	[26]
3	$CO_2 + M \longleftrightarrow CO + O + M$	6.9×10^{21}	−1.5	6.3275×10^4	H, O = 2.0, [26]
4	$CO_2 + O \longleftrightarrow O_2 + CO$	2.7×10^{14}	0.0	3.3797×10^4	[25]
5	$H + CO_2 \longleftrightarrow CO + OH$	1.6×10^{14}	0.0	1.32×10^4	[27]
6	$H + H_2O \longleftrightarrow H_2 + OH$	1.0×10^{10}	1.2	9.62×10^3	[27]
7	$H_2 + H \longleftrightarrow 2\,H + H$	8.5×10^{19}	−1.1	5.2335×10^4	[27]
8	$H_2 + H_2O \longleftrightarrow 2\,H + H_2O$	8.5×10^{19}	−1.1	5.2335×10^4	[27]
9	$H_2 + M \longleftrightarrow 2\,H + M$	9.0×10^{14}	0.0	4.840×10^4	H, H_2O = 0.0, [27]
10	$H_2 + O_2 \longleftrightarrow 2\,OH$	2.5×10^{12}	0.0	1.96×10^4	[27]
11	$H_2O + C \longleftrightarrow OH + H + C$	1.3×10^{21}	−1.0	6.0×10^4	[27]
12	$H_2O + H \longleftrightarrow OH + 2\,H$	1.3×10^{21}	−1.0	6.0×10^4	[27]
13	$H_2O + H_2O \longleftrightarrow OH + H + H_2O$	1.3×10^{21}	−1.0	6.0×10^4	[27]
14	$H_2O + M \longleftrightarrow OH + H + M$	1.3×10^{21}	−1.0	6.0×10^4	H, C, H_2O = 0.0, [27]
15	$H_2O + O \longleftrightarrow OH + H + O$	1.3×10^{21}	−1.0	6.0×10^4	[27]
16	$O + H_2 \longleftrightarrow OH + H$	3.9×10^4	2.7	3.15×10^3	[27]
17	$O + H_2O \longleftrightarrow 2\,OH$	3.4×10^{10}	1.0	8.6×10^3	[27]
18	$O_2 + M \longleftrightarrow 2\,O + M$	2.0×10^{21}	−1.5	5.936×10^4	C, O, H = 5.0, [28]
19	$OH + M \longleftrightarrow O + H + M$	2.4×10^{15}	0.0	5.0×10^4	[27]

Table 3 Engine plenum species mass fractions.

Species	Mass Fraction
H_2O	0.4009
CO_2	0.2698
H_2	0.0067
CO	0.2164
OH	0.0558
O_2	0.0413
O	0.0081
H	0.0010

B. Computational Approach and Grid Generation

All solutions are generated using FUN3D, an unstructured grid node-based finite-volume CFD solver developed at NASA Langley Research Center [29]. A finite-volume approach is used for spatial discretization on generic unstructured grids containing tetrahedra, pyramids, prisms, and hexahedra. The equations are integrated in time using an implicit formulation. For the thermochemical non-equilibrium path of FUN3D, turbulence and chemistry are solved fully coupled with momentum and energy. For this campaign, turbulence is modeled using SA-Catris DES [30, 31] and solved with a fully coupled methodology.

FUN3D is implemented in Modern Fortran and CUDA C++. This work primarily utilizes a stand-alone CUDA C++ library of FUN3D kernels called FLUDA, which enables the usage of NVIDIA GPU architectures [32]. This recent work has shown performance improvements for the thermochemical non-equilibrium path of more than an order of magnitude for an NVIDIA Tesla V100 over a typical x86 CPU node consisting of 40 physical cores. Details on the governing equations as well as numerical and software implementation can be found in Refs. [32, 33].

All grids are generated with GridEx [34], a NASA-developed tool to link geometry and grid generation, and AFLR3 [35]. All grids contain mixed elements, with prisms in the boundary layer (with a normal wall spacing of $y^+ \approx 1$), tetrahedra in the volume, and pyramid elements as required at interfaces. The main changes to the computational grids between this effort and the prior effort [15] is in the lack of scaling required in the nozzle geometry; all volume grid sources remain unchanged.

The fine grids used for this work are presented in Table 4. To generate the fine grids, coarse grids are generated using conventional methods, and then each edge is split in half to increase the overall number of points by approximately a factor of eight. The projection of new points introduced on the boundaries of the domain to the analytical CAD definition is done using a linear elasticity procedure [36] to smoothly interpolate these changes into the grid interior. The grid sources for each condition vary slightly, which leads to varying grid sizes. Most notably, the subsonic condition grid extends the upstream source further than the transonic and supersonic conditions, which leads to approximately 15% more points in the grid. As in the prior perfect-gas campaign, domain dimensions are most easily specified using units of kilometers, where the smallest flow features resolved are at centimeter length scales. More details on the grid generation approach and wall spacing are provided in Ref. [15]. Figure 4 shows a 139 million point grid surface, the coarse grid for the supersonic condiition, with considerably finer spacing around the flush, scarfed nozzle exit planes on the heatshield. Figure 5 shows a view of the 139 million point volume grid near the centerline, with the partial domain extent and volume sourcing visible. Use of volume sourcing was limited to the plume interference region and applied sparingly to minimize transitions in spacing within these regions of the domain.

Table 4 Grid information for the investigated conditions.

Case	Grid Points	Prisms	Tetrahedra	Pyramids
$M_\infty = 2.4$	1,106,828,365	359,560,576	5,544,029,784	360,792
$M_\infty = 1.4$	1,106,075,974	345,375,848	5,580,829,096	398,928
$M_\infty = 0.8$	1,268,121,765	320,252,824	6,627,609,528	420,336

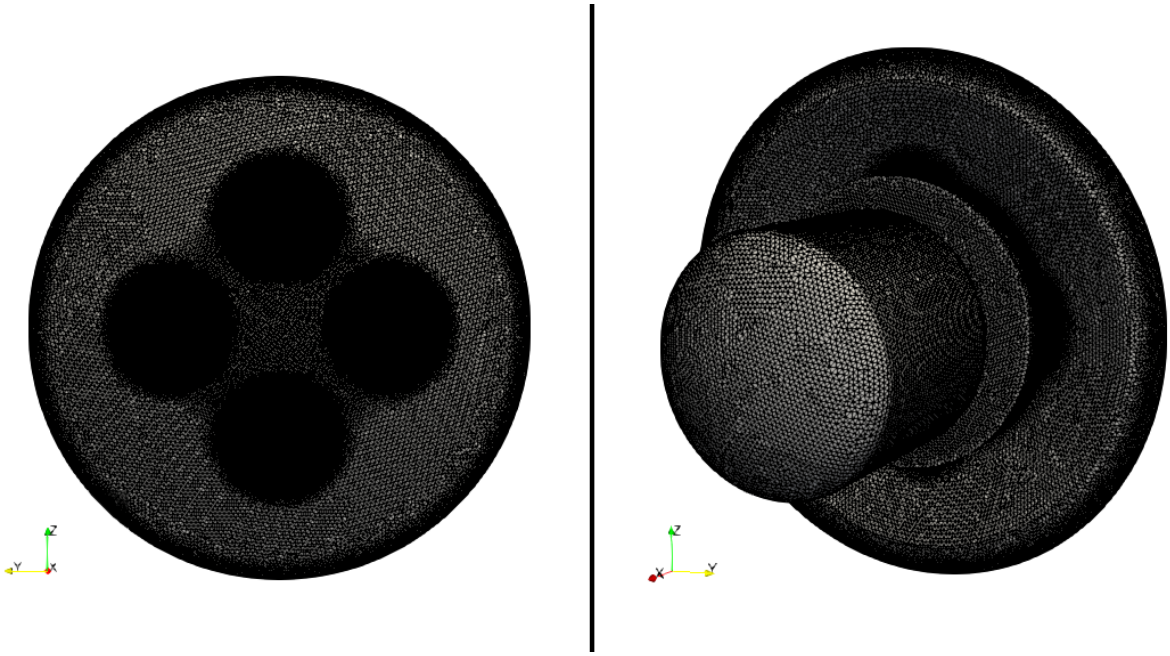

Fig. 4 Surface grid for 139 million point grid.

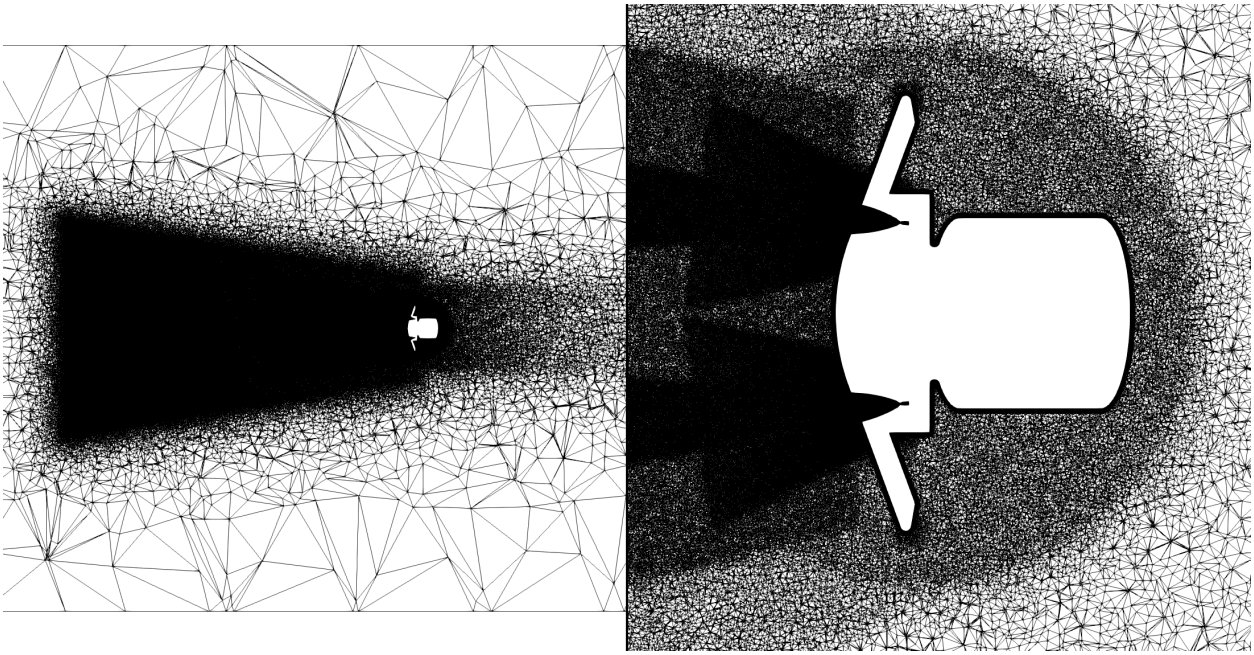

Fig. 5 Near-centerline slice of volume grid for 139 million point grid.

In all solutions, the full nozzle internal flow is modeled, beginning with the subsonic plenum, converging through the throat, and expanding through to the nozzle exit at the intersection with the heatshield. The supersonic freestream cases considered in this analysis do not have ratios of static pressure at the nozzle exit to post-shock freestream stagnation pressure much greater than unity at supersonic conditions, resulting in little margin in defining an individual nozzle as either over-expanded ($p_e < p_{0,2}$) or under-expanded ($p_e > p_{0,2}$). Computational simulation of plume-induced base environments for launch vehicles by Mehta et al. [37] concluded that accurate plume expansion and near-body effects such as convective heating and surface temperature require accurate modeling of the nozzle inner wall boundary

layer. As SRP flows are concerned with both far-field interference and immediate near-field body effects — and since quantifying the effect of finite-rate chemistry is an objective for this effort — simulation of the full nozzle and nozzle boundary layer ($\delta_{99} \approx 0.08R$ at the nozzle exit) is included and is shown in Fig. 6. As simulations increase in complexity through the addition of related disciplines, accurate prediction of surface quantities such as chemical composition, heat transfer, pressure, and shear stress is important for both the nozzles and the full vehicle. Resolving the turbulent flow directly adjacent to the vehicle offers a more first principles-based prediction of these quantities for future multiphysics analyses.

The nondimensional time step is fixed across the cases; there are 3417 time steps per reference time based on the heatshield diameter, $\tau = D/u_\infty$. The convective CFL number upstream of the vehicle is of order unity, and the global convective CFL number, neglecting effects of chemistry, which imposes further restrictions, based on the plena wall conditions ranges from 225 to 668 depending on the freestream conditions.

The solution start-up process utilizes two initialization volumes. The subsonic portion of the engine plena are initialized with subsonic outward flow at plena conditions. An additional spherical source around the vehicle with subsonic flow velocity at freestream density and temperature is also applied. Global time stepping is done for 50,000 time steps using 1 subiteration, and then 5 subiterations after that, achieving 3-5 orders of magnitude reduction for all equations. The fine grid solution is interpolated from the coarse grid solution and the same subiteration strategy is applied. Nozzles reach quasi steady state before the time-accurate phase of time stepping.

Fig. 6 Centerline slice of a nozzle for 139M point grid. The transparent gray surface indicates the scarfed nozzle walls.

C. Computational Performance

Summit [23] is an IBM architecture consisting of dual-socket 22-core POWER9 host processors and six NVIDIA Tesla V100 GPUs per compute node. In total, the system consists of 4,608 nodes. Ref. [32] details weak scaling performance on the system using the proposed modeling approach. Compared to perfect-gas flows, the current modeling approach is over an order of magnitude more expensive computationally. Weak scaling performance was carried out by fixing the grid points per node to 1.2 million (200,000 points per GPU) and running a few time steps for computational statistics. The scaling was performed separately for the CPUs and GPUs of the nodes. In summary, the GPUs show a consistent speedup of 72-84× per node relative to the CPUs, which implies a single GPU is approximately 13× faster than a dual-socket CPU. These numbers suggest that the throughput achieved by the GPUs running on 20% of Summit, 922 nodes, is comparable to approximately 3 million IBM POWER9 cores. However, it is worth noting that the implementation has not been optimized for the POWER9 architecture as discussed in [32].

The cases considered are run in various configurations as presented in Table 5. While the nondimensional time step is fixed across the cases, the corresponding physical time step is not. The physical time step increases as velocity is reduced. Because of this increase, the global CFL, governed by the plena walls, is scaled by the same ratio since the engine conditions are held fixed. The supersonic condition is run on 20% of Summit, or 922 nodes, and the average wall time of a nominal time step, which includes I/O, is 1.18 seconds. The transonic and subsonic conditions are strong scaled to approximately 80,000 points per GPU, and the wall time per time step is approximately half that of the supersonic case. The total simulation times for 300,000 time steps are approximately 4 days for the supersonic condition, and approximately 2 days for the transonic and subsonic conditions. The overall efficiency of the strong scaled runs is approximately 77% compared to the baseline run on 922 nodes. The grid used for the subsonic case is slightly larger than that of the transonic case and thus more nodes are used to maintain the nominal number of points per

GPU. The transonic and subsonic cases are run on approximately 50% and 58% of Summit, respectively. The wall time per time step per degree of freedom, which is considered a grid point in this scenario, is also computed in the table. This quantity is then scaled to determine the wall time for one second of simulation time. For the subsonic case, a value of 1.89×10^{-5} implies a wall time of approximately 5 hours to simulate one second of physical time using a grid containing one billion points partitioned to 80,000 points per GPU.

In the current implementation, the primary contributions to the cost of a nominal subiteration of the implicit dual time-stepping scheme include the computation of the residual, or flux balance (∼20%); the linearization of the residual (∼50%); and the solution of the associated linear system of equations (∼30%). For the purposes of the current discussion, this baseline cost is considered 1 time unit. However, in practice, the residual linearizations are updated less frequently as the nonlinear solution converges, such that a physical time step requiring 5 subiterations typically costs about 4 time units.

Based on this analysis, a four-stage explicit scheme would be expected to cost 0.8 time units per physical time step, or approximately one-fifth that of the implicit scheme. However, stability requirements limit the explicit scheme to global convective CFL numbers of approximately unity, ignoring further restrictions imposed by chemistry-related concerns. This value stands in stark contrast to those ranging from 225 to 668 shown in Table 5. The explicit approach is therefore estimated to require 45-134× more wall time than the implicit formulation for a fixed temporal duration. While the implicit approach requires approximately 5 hours to compute the subsonic scenario presented above, a four-stage explicit scheme is expected to require roughly 28 days for an equivalent simulation.

Table 5 Performance summary for the nominal campaign cases.

Case	Time Step [μs]	Global CFL	GPUs	Points / GPU	Wall Time [s] / Time Step	Wall Time [s] / Time Step / DOF	Wall Time [s] / DOF / Second of Simulation Time
$M_\infty = 2.4$	8.6	225	5,532	200,000	1.18	1.07×10^{-9}	1.25×10^{-4}
$M_\infty = 1.4$	14.6	384	13,824	80,000	0.62	5.61×10^{-10}	3.85×10^{-5}
$M_\infty = 0.8$	25.4	668	15,912	80,000	0.61	4.81×10^{-10}	1.89×10^{-5}

IV. Results and Discussion

Results and discussion are focused on observations of the effect of including finite-rate chemistry in full-scale, DES solutions on flowfield structure, composition, and integrated aerodynamic forces and moments. The solutions each fix the individual engine thrust at 80% throttle and are presented for freestream Mach numbers of 2.4, 1.4, and 0.8, more detailed conditions for which are specified previously in Table 1. A comparison to prior perfect-gas (air) results is included for the Mach 2.4 condition, as this is the closest physical comparison in terms of both thrust and pressure ratio ($p_e/p_{0,2}$). For the other conditions, the thrust of the reacting-gas cases are much larger than the perfect-gas cases. The perfect-gas campaign is developed to match experimental wind tunnel conditions which investigate various pressure ratios. As mentioned previously, the vehicle maintaining constant high throttle is a realistic scenario for an actual flight [24]. In addition, previous perfect-gas scaling assumptions breakdown with finite-rate chemistry which leads to ambiguity regarding the similarity parameters such as pressure ratio, which now depends on finite-rate chemistry and cannot be computed analytically.

A. Mach 2.4 Conditions

Recent human Mars vehicle performance analyses initiate powered descent near Mach 2.4. While this initiation condition will vary with changes to the required payload mass and with increases or decreases in the available engine thrust, the Mach 2.4 condition remains representative of potential mid-supersonic conditions where a strong, detached shock forms upstream of the flow obstruction. In the retropropulsion case, this shock is displaced considerably further upstream, ahead of the vehicle, than is the case for the same vehicle at the same conditions with no retropropulsion.

The time step is approximately 8.56 μs, which yields a total integration time of 4.45 seconds after 520,000 time steps. The simulation is run on 922 Summit nodes, 20% of the system, for a little over 7 days of run time (see Section III.C for more details on performance). Figure 7 shows instantaneous contours of the flowfield for the reacting-gas simulation in

the Z-plane. Qualitatively, these flow structures are consistent with those observed in the perfect-gas-scaled case from the prior effort, with instantaneous Mach number contours and vorticity magnitude volume rendering shown in Fig. 8.

The flowfield asymmetry visible in the perfect-gas Mach number contours in Fig. 8, persisting through the 275,000 time steps completed, also occurs in the reacting-gas case, though in the Y-plane, not the Z-plane. In the reacting-gas case, however, the flowfield returns to a much more symmetric structure after approximately 250,000 time steps and remains so through the next 270,000 time steps completed. The displacement of a strong shock upstream is evident in Fig. 7, as is an abundance of mixing both between the visible plumes and in the region between the termination of the jet core flow and the upstream shock. In looking at the pressure contours, the plumes can be seen to be under-expanded, as expected for these conditions due to the pressure ratio, $p_e/p_{0,2}$, where $p_{0,2}$ has been used to approximate the local pressure at the nozzle exit, and proximity of the neighboring plume in the paired nozzle configuration. Characteristically thick, turbulent shear layers are visible in Fig. 7, particularly in comparing the Mach number and temperature contours with the pressure contours, as the plume shape is defined by a matched pressure boundary. For slightly lower thrust conditions, the plumes become over-expanded, which consequently lead to significant pressure recovery on the heatshield. This lower thrust supersonic condition of the current campaign is detailed in Ref. [18].

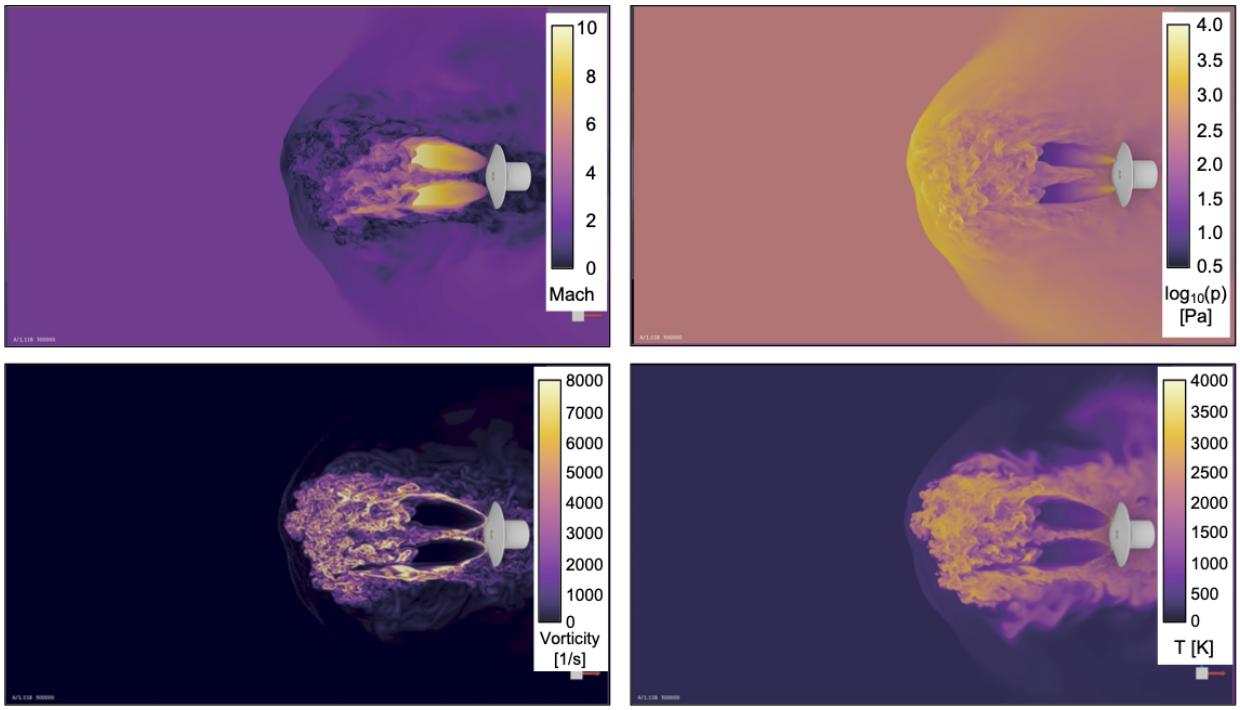

Fig. 7 Z-plane views of instantaneous flowfield contours at $t \approx 2.5$ s for Mach number, pressure (log scale), vorticity magnitude, and temperature - M_∞ = 2.4, reacting-gas simulation.

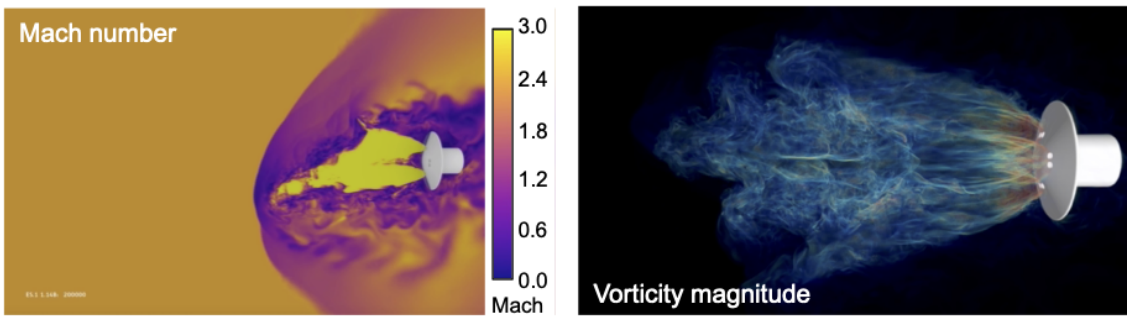

Fig. 8 Z-plane view of instantaneous Mach number contours and volume-rendered vorticity magnitude - M_∞ = 2.4, perfect-gas simulation (from [14]).

Figure 9 shows the same Z-plane instantaneous flowfield view using species mass fraction contours for CO_2, CO, H_2O, and OH. The freestream Martian atmosphere is predominantly CO_2, and the primary products of combustion for this engine are CO_2 and H_2O. Significant after-burning, or chemical reactions external to the nozzles, is visible in the mass fractions shown for CO and OH. The temperature contours in Fig. 7 are consistent with the composition in Fig. 9. Significant reactions are occurring between the plumes and in the mixing region between the oncoming and opposing flows. The mass fraction of OH, in excess of 4%, is significant in comparison to other supersonic combustion problems, where it generally is found to be a minor product.

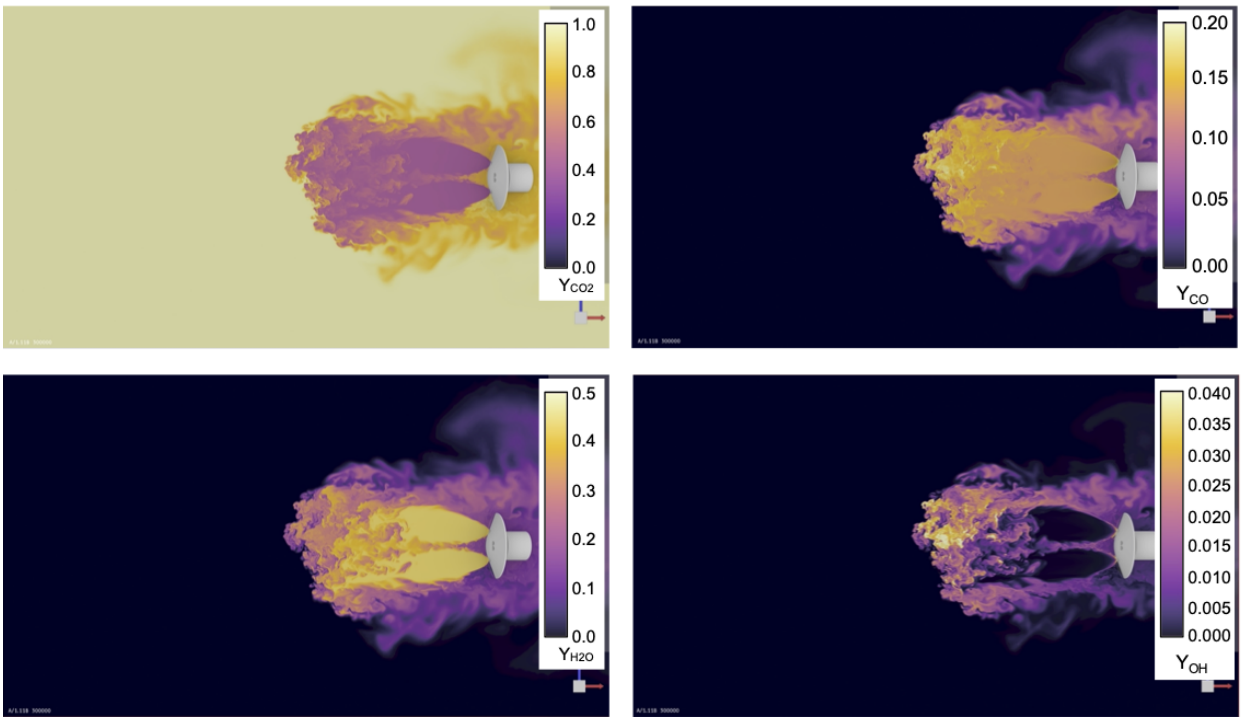

Fig. 9 Z-plane views of instantaneous flowfield contours at $t \approx 2.5s$ for mass fractions of CO_2, CO, H_2O, and OH - M_∞ = 2.4, reacting-gas simulation.

From the standpoint of vehicle performance, the external flowfield can be highly complex, with highly non-stationary flow features, but if this does not translate into variations in surface pressure and in integrated forces and moments on the vehicle, it will have minimal impacts to vehicle stability and control. Figure 10 shows a series of instantaneous C_p contours on the vehicle heatshield in increments of 0.21 s (25,000 time steps). The off-body flowfield unsteadiness leads to significant variations in surface pressure over large areas of the heatshield. Regions of higher and lower pressures do not remain localized, with the largest variations seen outboard of the nozzles and appearing in every quadrant through

out the series of instantaneous views in Fig. 10. Figure 11 shows the mean C_p distributions on the heatshield for both the perfect-gas case and the reacting-gas case. The averaging interval for the perfect-gas solution is 100,000 time steps, and the averaging interval for the reacting-gas solution is 200,000 time steps, where the reacting-gas solution has a longer temporal history than the prior perfect-gas solution. It is interesting to note that, similar to the perfect-gas solution, a large asymmetry in the flowfield plume structure is also observed in the reacting-gas solution through this averaging interval but in a different plane. The asymmetry disappears completely in the reacting-gas case as the solution is run longer. No elevated pressures inboard of the nozzles from the post-shock pressure recovery are observed, which is consistent with the inboard plume shear layer interactions shown in Figs. 7 and 9.

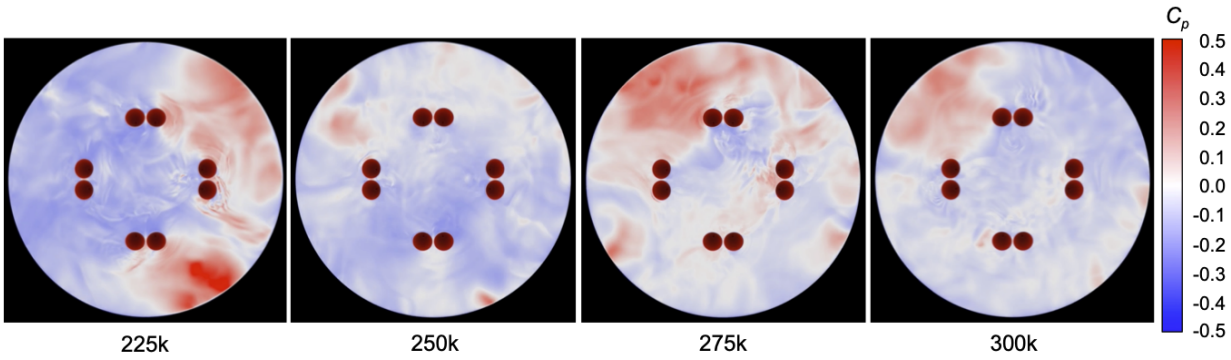

Fig. 10 Time series of forebody C_p contours from reacting-gas simulation - M_∞ = 2.4.

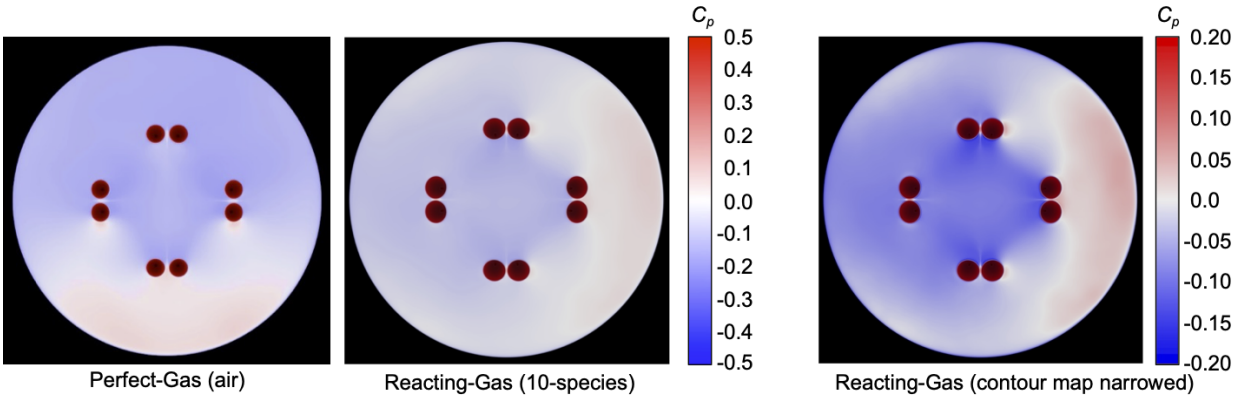

Fig. 11 Comparison of heatshield mean C_p distribution between perfect-gas (air) and reacting-gas simulations - M_∞ = 2.4.

In addition to flowfield structure and behavior comparisons, the aerodynamic forces and moments resulting from retropropulsion interference are of primary interest in understanding and quantifying vehicle-level impacts. Figure 12 shows the full time-history for the vehicle aerodynamic forces and moments for the reacting-gas case, and Fig. 13 shows the full-time history for the perfect-gas case. The moment reference point is the physical center, or nose, of the heatshield. As may be expected from the flowfield shown in Fig. 7, the axial force coefficient is substantially reduced from what would be expected for a 70° sphere-cone at supersonic conditions (C_A of approximately 1.7) due to the large freestream flow obstruction created by the retropropulsion exhaust plumes. Comparing the C_A histories, the mean C_A for the heatshield and for the full vehicle is noticeably higher in the reacting-gas case than in the perfect-gas case. At mid-supersonic conditions, an increase in axial force for blunt vehicle shapes due to elevated aftbody surface pressures is to be expected.

Given that the vehicle is flying at a 0° angle of attack, the expectation is that all moments and the y- and z- force components should yield a mean very near zero. The perfect-gas time histories show the offset from zero in pitching moment due to the flowfield asymmetry described previously. A similar offset, but in the yawing moment is visible

earlier in the time history for the reacting-gas case, but beyond approximately 2.4 s of physical time simulated, the flowfield becomes symmetric and remains symmetric through the duration of the run. In all components, high-frequency unsteadiness is observed, with some indication of potential lower frequency behavior as well that will require a longer time duration to resolve. It is the temporal variation in the forces and moments that potentially present challenges to vehicle stability and control in a flight implementation.

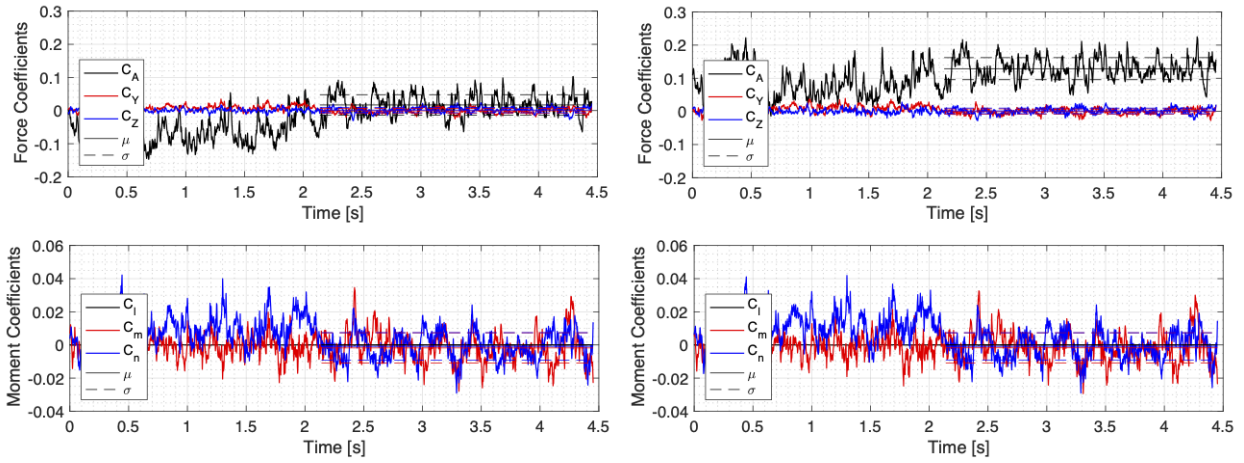

(a) Forebody Only (b) Full Vehicle (total)

Fig. 12 Aerodynamic force and moment history for the (a) forebody and (b) full vehicle - Mach 2.4, reacting-gas.

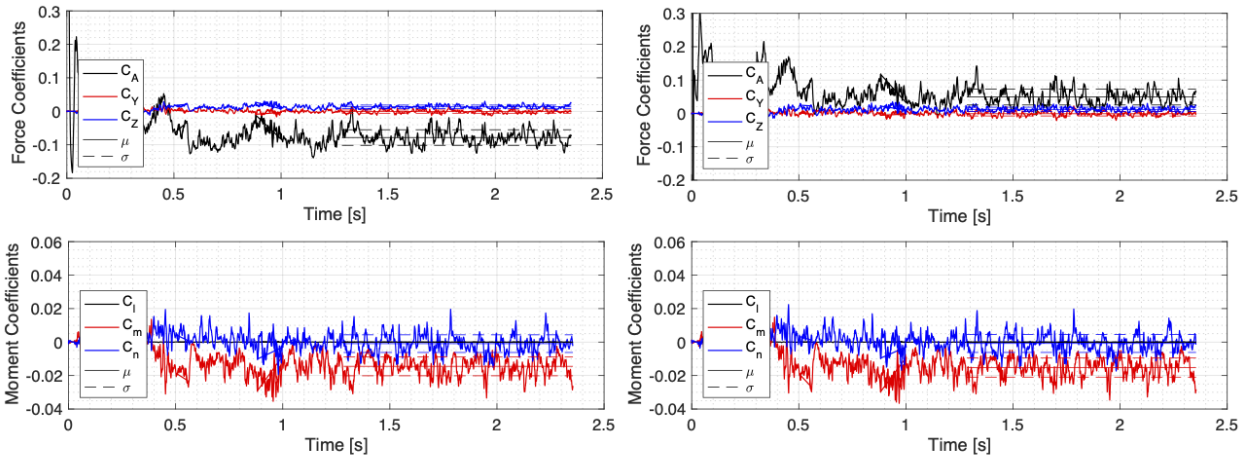

(a) Forebody Only (b) Full Vehicle (total)

Fig. 13 Aerodynamic force and moment history for the (a) forebody and (b) full vehicle - Mach 2.4, perfect-gas.

Supersonic conditions, due to the potential for substantial pressure recovery across the bow shock and plume structures to reduce the obliqueness of this shock inboard of the nozzles, are the mostly likely portion of powered flight for aerodynamic contributions to deceleration to be significant. In this specific case, while the plumes never fully coalesce inboard of the nozzles, there is considerable mixing of the proximal shear layers, preventing elevated pressures post-shock from reaching the vehicle forebody. The mean and standard deviation of the axial aerodynamic force coefficient for the vehicle at Mach 2.4 are 0.1289 and 0.0333, respectively, and the total thrust coefficient (axial component) is 2.3305. Aerodynamic contribution to deceleration at these conditions is 5.24%. To improve the averaging interval for the comparable perfect-gas case, an additional 75,000 time steps were run beyond the prior reported duration. With the limitations of scaling to air and using perfect-gas assumptions, the mean and standard deviation of the axial

aerodynamic force coefficient are 0.0492 and 0.0512, respectively. The perfect-gas C_T is 3.0975, and the aerodynamic contribution to deceleration at these conditions is 1.56%. With under-expanded plumes, a higher C_T is expected to produce a larger plume structure, as will the higher ratio of specific heats for air in the limit where the approximation for the local pressure at the nozzle exit does not adequately match pressure ratio between the perfect-gas and reacting-gas cases. Even with a 5.24% aerodynamic contribution to the total deceleration force with the inclusion of reacting-gas chemistry, the retropropulsive thrust dominates the deceleration force on the vehicle.

B. Mach 1.4 Conditions

The vehicle decelerates from Mach 2.4 to Mach 1.4 after 19 seconds of powered flight, and at Mach 1.4, the dynamic pressure is half the supersonic condition (see Table 1). The engine throttle level is maintained at 80%, with identical engine chamber pressure and temperature as used for the mid-supersonic condition. The time step is approximately 14.6 μs, which yields a total integration time of 4.38 seconds after 300,000 time steps. This case is strong scaled compared to the supersonic condition and is run with approximately 80,000 grid points per GPU. The simulation is run on 2304 Summit nodes, half the system, for a little over 2 days of run time (see Section III.C for more details on performance). The flowfield reaches a statistically stationary state after approximately 1.5 seconds into the simulation.

Figure 14 shows instantaneous contours of the flowfield for the reacting-gas simulation in the Z-plane. Qualitatively, the flow structures are characteristically similar to those shown previously in Fig. 7, but the diminishing strength of the upstream shock and the reduced dynamic pressure are becoming apparent in the increased upstream extent of the exhaust plumes. The mean bow shock stand-off distance increases to approximately 105 meters ($\approx 6.4D$), over 2$\times$ larger than the mean stand-off distance for the Mach 2.4 condition. While still under-expanded, the individual plumes are narrower than in Fig. 7 and have shallower flow turning angles in matching the local pressure field. Asymmetric transients as seen in the mid-supersonic condition are not present in this case.

Figure 15 shows the same Z-plane instantaneous flowfield view using species mass fraction contours for CO_2, CO, H_2O, and OH. Chemical reactions external to the nozzles are apparent, though the temperatures are lower than in the Mach 2.4 case. Hydroxl radical mass fractions are similar to the mid-supersonic condition, reaching peak values of 4% upstream of the vehicle. The plume shear layers interact with both neighboring and cross-body plumes, leading to increased mixing and consequently chemical reactions.

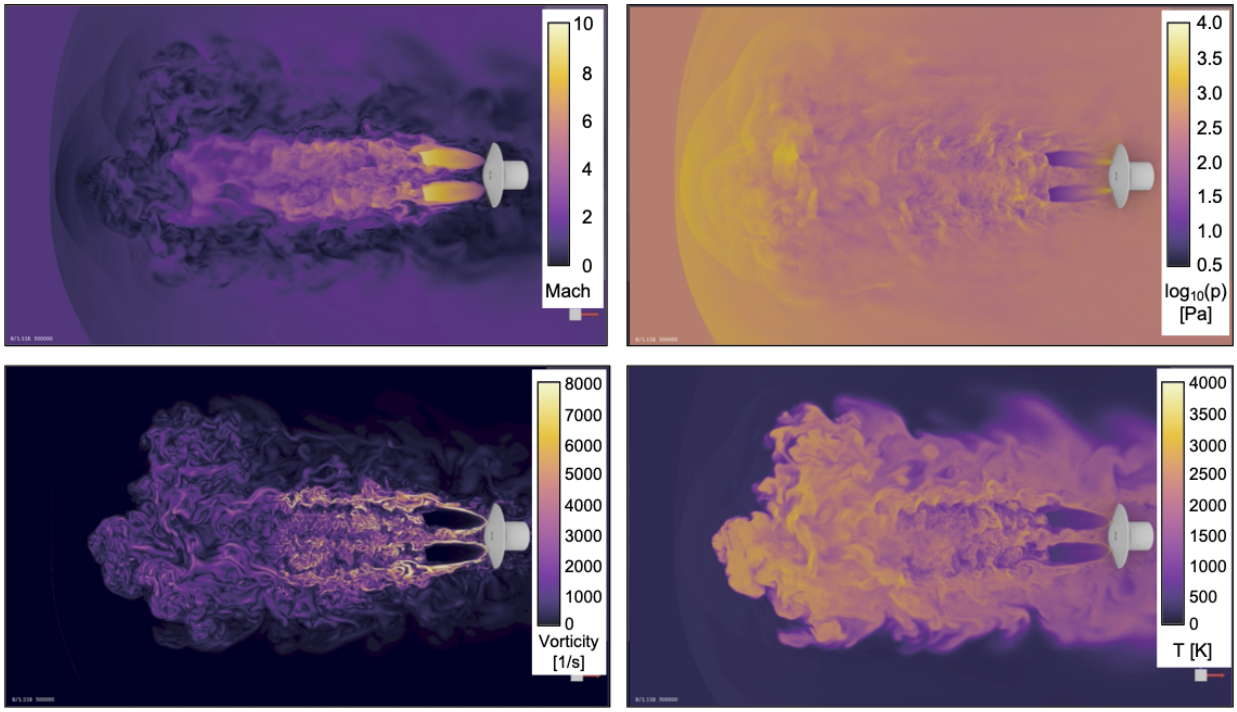

Fig. 14 Z-plane views of instantaneous flowfield contours for Mach number, pressure (log scale), vorticity magnitude, and temperature - M_∞ = 1.4, reacting-gas simulation.

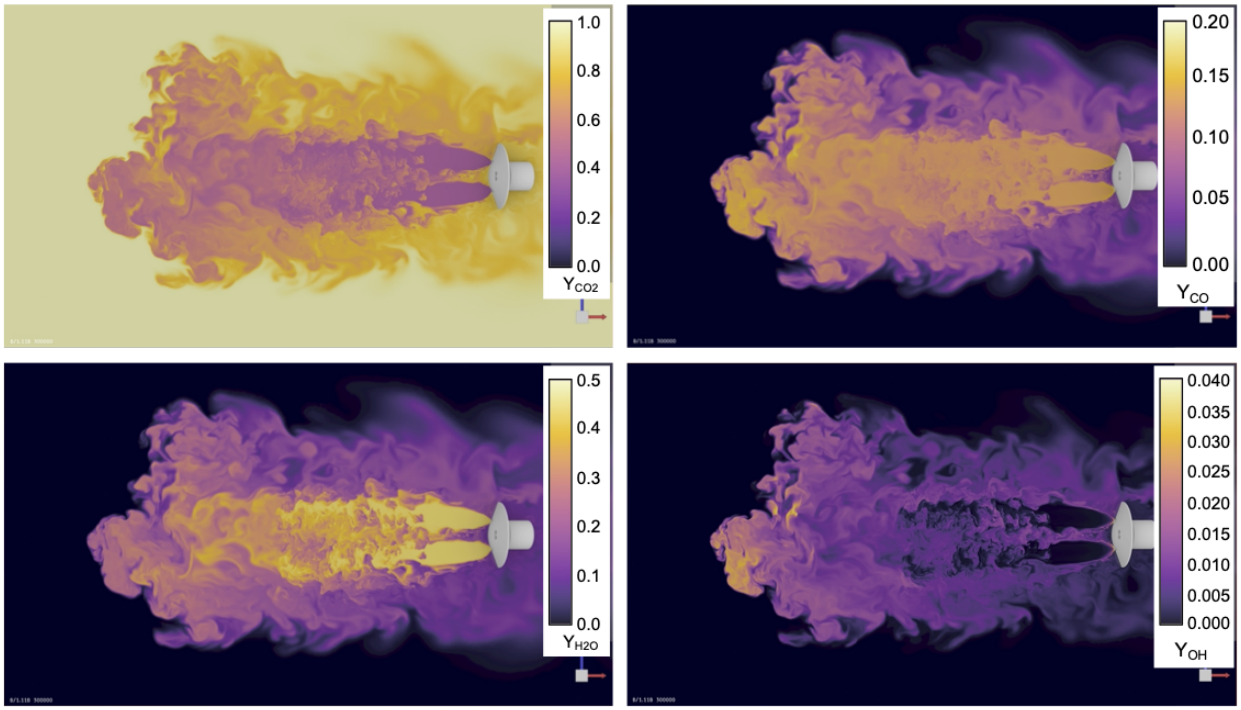

Fig. 15 Z-plane views of instantaneous flowfield contours for mass fractions of CO_2, CO, H_2O, and OH - M_∞ = 1.4, reacting-gas simulation.

Figure 16 shows a series of instantaneous C_p contours on the vehicle heatshield in increments of 0.36 s (25,000 time steps). Regions of higher and lower pressures do not remain localized, and similar to the Mach 2.4 case, significant variations in surface pressure are arising from the off-body flowfield unsteadiness. No elevated pressures inboard of the nozzles from the post-shock pressure recovery are observed, which is consistent with the inboard plume shear layer interactions shown in Figs. 14 and 15 and weakening of the upstream-displaced bow shock.

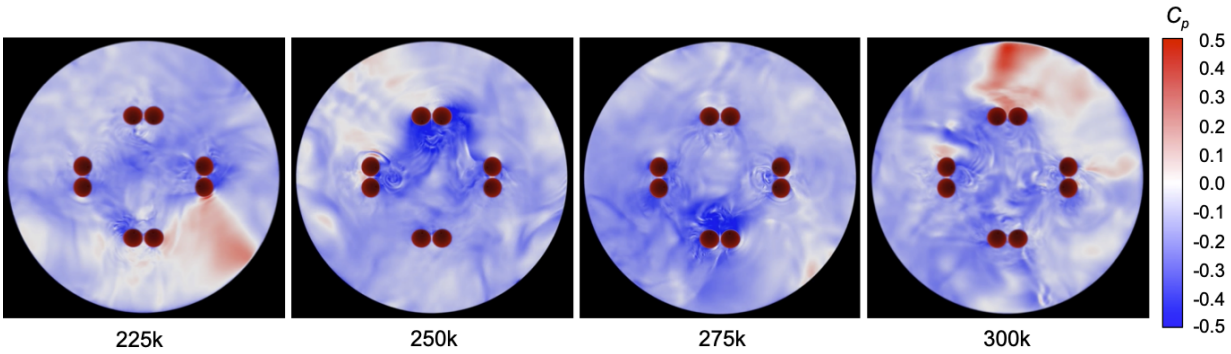

Fig. 16 Time series of forebody C_p contours from reacting-gas simulation - M_∞ = 1.4.

Figure 17 shows the full time-history for the vehicle aerodynamic forces and moments for this transonic, reacting-gas case. The mean and standard deviation are indicated by solid and dashed lines, respectively, with the averaging interval taken from 100,000 time steps to the end of the simulation. Given the far-upstream displacement of the bow shock by the plume structures (see Fig. 14), the minimal freestream post-shock pressure recovery is not expected to reach the vehicle forebody. The integration of pressures below that of the freestream yields the negative forebody axial force coefficient values shown in Fig. 17. As in the supersonic case, the full vehicle axial force coefficient includes a positive contribution from the pressure increment on the aft surfaces of the vehicle. As no gross flowfield asymmetry is observed

in this transonic case, the normal and side force and pitching and yawing moment histories have mean values very close to zero.

The axial aerodynamic force coefficient of the vehicle is therefore not expected to be significant compared to the axial thrust coefficient. The mean and standard deviation of the axial aerodynamic force coefficient for the vehicle are 0.0368 and 0.0374, respectively. The total thrust coefficient (axial component) is 5.016; aerodynamic contribution to deceleration at these conditions is 0.73%. The total axial coefficient, the sum of the aerodynamic and thrust coefficients, is thus primarily due to the thrust of the engines.

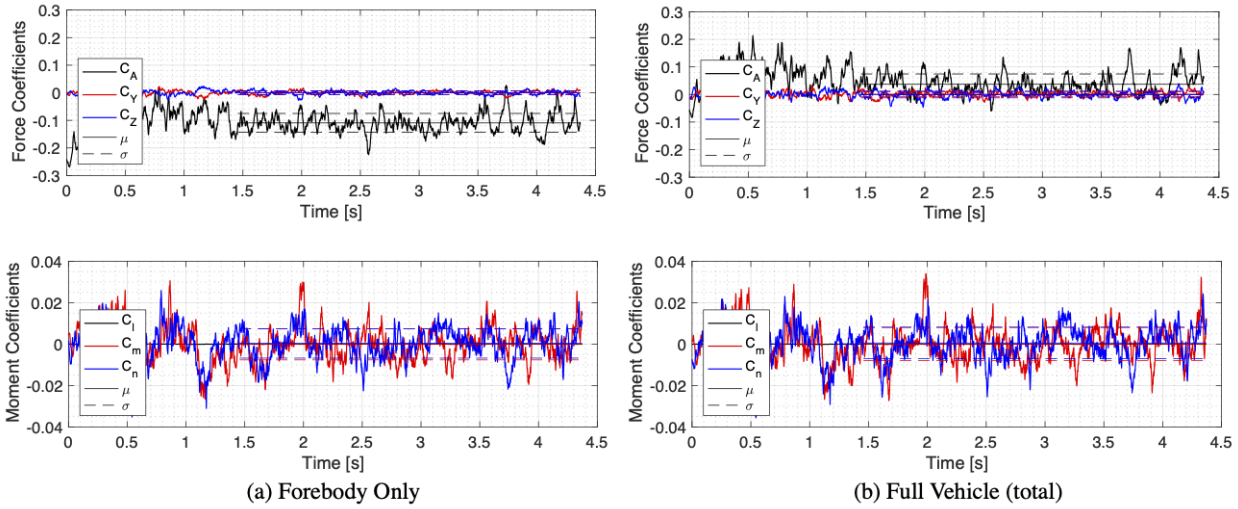

(a) Forebody Only (b) Full Vehicle (total)

Fig. 17 Aerodynamic force and moment history for the (a) forebody and (b) full vehicle - Mach 1.4, reacting-gas.

C. Mach 0.8 Conditions

The vehicle decelerates from Mach 1.4 to Mach 0.8 after an additional 12 seconds of powered flight, or 31 seconds after engine initiation at Mach 2.4. At Mach 0.8, the dynamic pressure is 20% of that at the supersonic condition, and 40% of that at the transonic condition (see Table 1). The engine throttle level is maintained at 80%, with identical engine chamber pressure and temperature as used for the mid-supersonic and transonic conditions, representative of an actual vehicle descent. The time step is approximately 25.4 μs, which yields a total physical integration time of 7.62 seconds after 300,000 time steps. Because the plumes extend so far upstream in this case, the grid was updated to extend the volume grid sourcing further upstream. The resulting grid has approximately 15% more points than the transonic and supersonic condition grids, and the domain extends seven heatshield diameters upstream of the vehicle. To maintain a similar computational load to the that of the transonic condition case, more Summit nodes are utilized. This subsonic case is run on 2652 nodes with nearly 16,000 GPUs (see Section III.C for more details on performance). Run time is essentially identical to the transonic case since the computational load is identical. The flowfield reaches a statistically stationary state after approximately 2 seconds of simulation time.

Figure 18 shows instantaneous contours of the flowfield for the reacting-gas simulation in the Z-plane. Qualitatively, the flow structures are characteristically similar to those shown previously in Fig. 14, even with no bow shock present due to the subsonic freestream condition. As expected, with no upstream shock to increase the local pressure at the nozzle exit, the plumes are thinner and extend much further upstream than in the supersonic case.

Figure 19 shows the same Z-plane instantaneous flowfield view using species mass fraction contours for CO_2, CO, H_2O, and OH. As in both the supersonic and transonic cases, chemical reactions external to the nozzles are apparent. Hydroxl radical mass fractions are less than those at the supersonic and transonic conditions, reaching peak values of 1% upstream of the vehicle. This difference is primarily attributed to the near plume structure; the peak Mach number at the Mach disk is lower than that for the transonic case, leading to reduced temperatures post Mach disk. The plume shear layers interact with both neighboring and cross-body plumes, leading to increased mixing and consequently chemical reactions. Asymmetric transients as seen in the supersonic case are not present in this case.

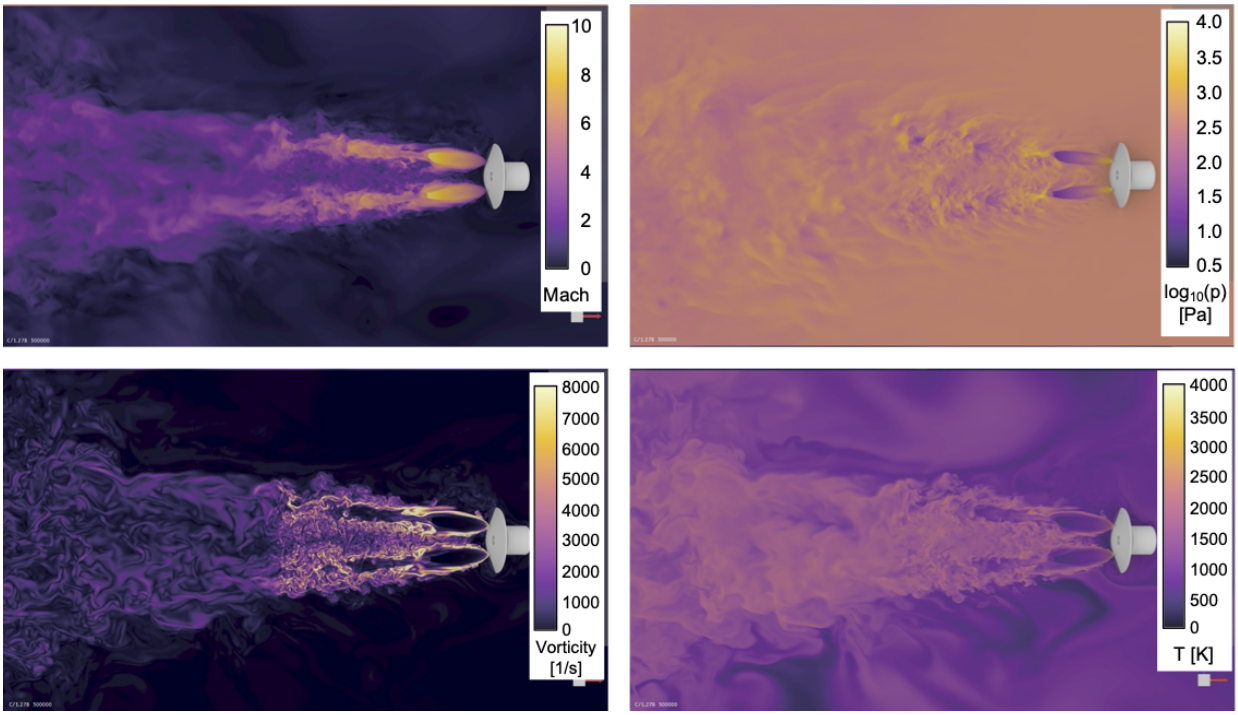

Fig. 18 Z-plane views of instantaneous flowfield contours for Mach number, pressure (log scale), vorticity magnitude, and temperature - M_∞ = 0.8, reacting-gas simulation.

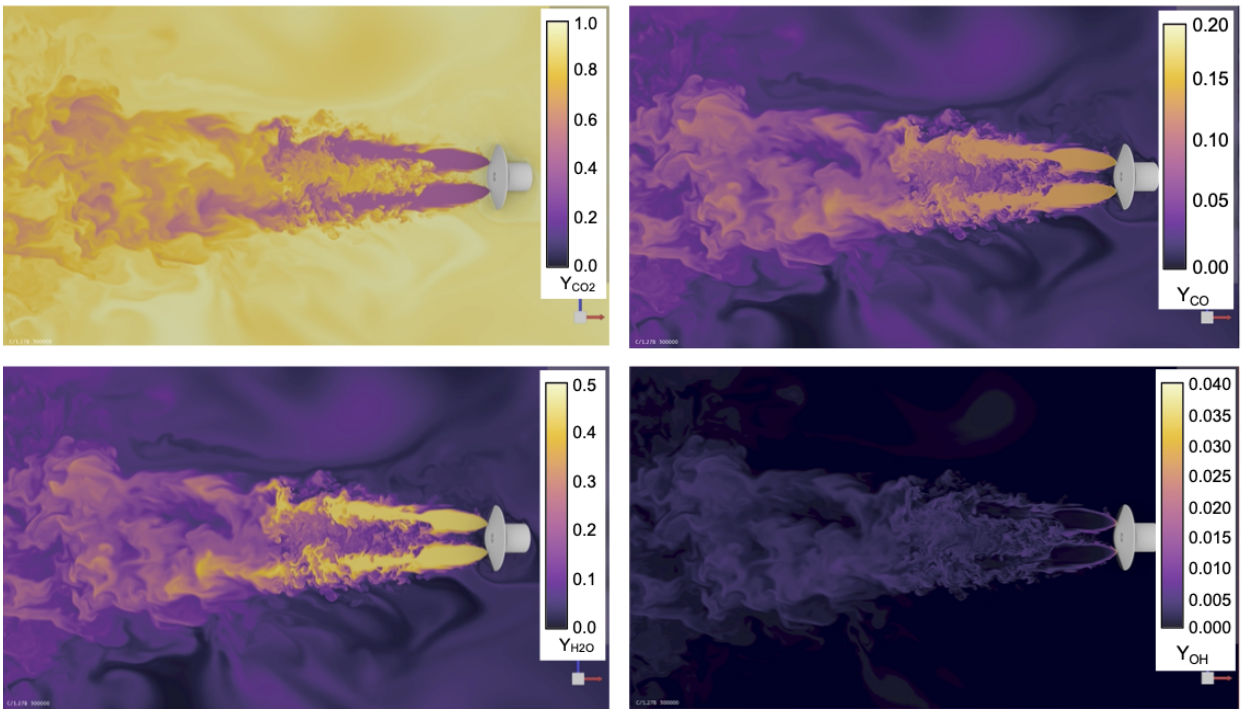

Fig. 19 Z-plane views of instantaneous flowfield contours for mass fractions of CO_2, CO, H_2O, and OH - M_∞ = 0.8, reacting-gas simulation.

Figure 20 shows a series of instantaneous C_p contours on the vehicle heatshield in increments of 0.64 s (25,000 time steps). Regions of higher and lower pressures do not remain localized, and similar to the Mach 2.4 and Mach 1.4 cases, significant variations in surface pressure are arising from the off-body flowfield unsteadiness. No elevated pressures inboard of the nozzles are present, as is expected with no shock upstream of the vehicle.

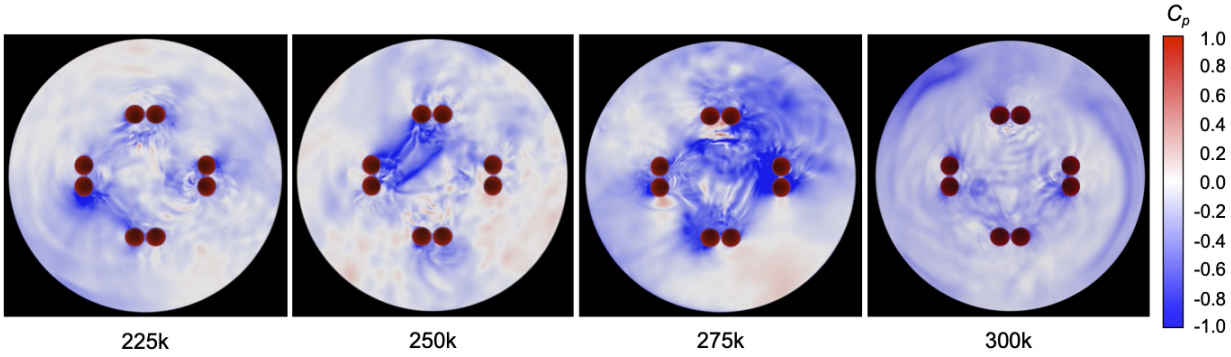

Fig. 20 Time series of forebody C_p contours from reacting-gas simulation - M_∞ = 0.8.

Figure 21 shows the full time-history for the vehicle aerodynamic forces and moments for this subsonic, reacting-gas case. The mean and standard deviation are indicated by solid and dashed lines, respectively, with the averaging interval taken from 100,000 time steps to the end of the simulation. Given the lack of bow shock at these subsonic conditions (see Fig. 18), no freestream post-shock pressure recovery is possible, and the flow entrainment over the outboard forebody surfaces reduces the surface pressure considerably. The integration of pressures below that of the freestream yields the negative forebody axial force coefficient values shown in Fig. 21. As in the supersonic and transonic cases, the full vehicle axial force coefficient includes a positive contribution from the pressure increment on the aft surfaces of the vehicle. As no gross flowfield asymmetry is observed in this subsonic case, the normal and side force and pitching and yawing moment histories have mean values very close to zero.

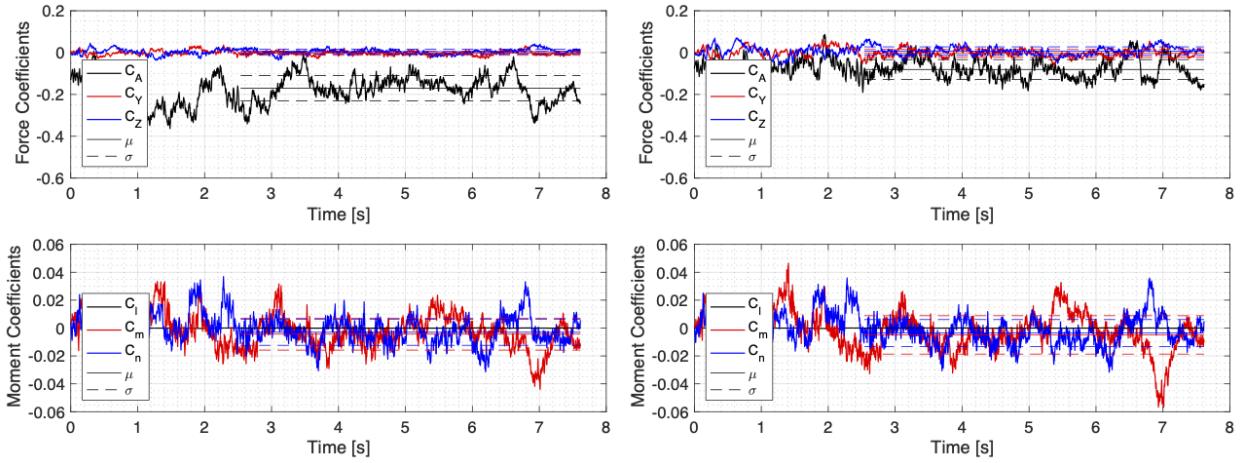

Fig. 21 Aerodynamic force and moment history for the (a) forebody and (b) full vehicle - Mach 0.8, reacting-gas.

The mean and standard deviation of the axial aerodynamic force coefficient for the vehicle at Mach 0.8 are -0.0805 and 0.0471, respectively, and the total thrust coefficient (axial component) is 13.3310. Aerodynamic contribution to deceleration at these conditions is -0.60%. Because the flowfield has subsonic freestream conditions, there is no longer a shock upstream of the vehicle and accordingly, no potential pressure recovery. In addition, significant entrainment is visible in the instantaneous flowfield contours over the portions of the heatshield outboard of the nozzles, decreasing the surface pressure. The reduction in surface pressure on the forebody is not overcome by the aftbody pressure increment,

resulting in a negative aerodynamic contribution to the total deceleration force on the vehicle. While the magnitude of this negative mean C_A is small, the implication is the potential for vehicle performance analyses to over-predict the available deceleration force on the vehicle in the absence of what is effectively a decrement to retropropulsion performance.

D. Additional Discussion

In this analysis, the engine thrust is held constant across all freestream conditions (Mach 2.4 to 0.8) by fixing chamber pressure, temperature, and initial composition. This, along with the fixed 0° angle of attack, is consistent with recent vehicle performance analyses as well as objectives to most efficiently maximize payload delivered to the surface. The vehicle loses little altitude during this initial portion of powered descent, and fixing engine thrust across the supersonic-to-transonic-to-subsonic speed range permits observation of the effects of changing freestream Mach number and dynamic pressure (see Table 1). Figure 22 shows the change in bow shock standoff distance and in the exhaust plume structure for all three trajectory points simulated.

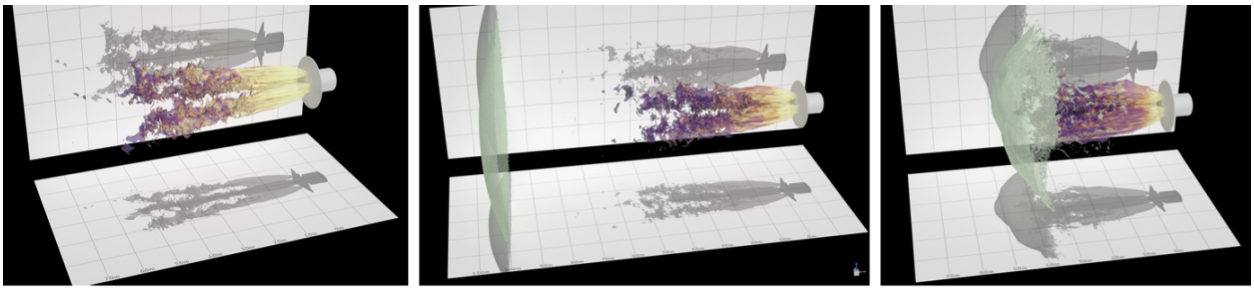

Fig. 22 Reacting-gas H_2O mass fraction isosurfaces (40%) colored by vorticity magnitude with bow shock visualized by a shock sensor based on Ref. [38].

The mean bow shock standoff distance more than doubles from the supersonic to transonic condition, and plume structure variations are also apparent as the flow becomes increasingly less under-expanded. The plumes become thinner and longer as the freestream Mach number decreases, and the local pressure field is increasingly less influenced by the upstream shock (and not at all in the subsonic case). The plumes extend more than five heatshield diameters upstream for the subsonic condition. Figure 23 shows the mean C_p distributions on the vehicle heatshield for all three freestream conditions. Consistent with the resulting flow structures and influence of the upstream shock on the local pressure field, surface pressures on the forebody are highest at supersonic conditions and decrease with the reduction in available post-shock pressure recovery. Tables 6 and 7 summarize the forebody and total aerodynamic force and moment coefficient statistics, as well as the aerodynamic contribution to the total axial deceleration force on the vehicle. As noted in the prior sections, the aerodynamic contribution, even with the signficant standard deviations in Table 6, to the total deceleration force on the vehicle is still dominated by thrust.

An objective of this analysis was to examine the effect of including finite-rate chemistry in the simulation of retropropulsion flows. In the three cases simulated, there are significant chemical reactions that occur upstream of the vehicle. Hydroxl mass fractions peak in excess of 4% for the supersonic and transonic conditions, and afterburning is observed throughout the interaction region. There are also significant variations in specific heat ratio through the flowfield, including the internal nozzle flow.

There are engineering modeling questions regarding pseudo-species that should be investigated in future work to determine their overall impact on vehicle performance, such as the accuracy of any retained temperature dependence on thermodynamic properties. At a minimum, the pseudo-species approaches should have temperature-dependent properties to accurately simulate the highly temperature-dependent CO_2 present in both the engines and the Martian atmosphere. Figure 24 shows mean contours for the specific heat ratio from the supersonic case and the internal nozzle flow for 80% throttle conditions. The specific heat ratio in the engines varies from approximately 1.19 to 1.26. Assuming a constant specific heat ratio directly impacts the upstream flowfield. The peak Mach number at the Mach disk is approximately 10. For a specific heat ratio of 1.19 using isentropic normal shock relationships, the stagnation to static temperature ratio is 10.5; for a specific heat ratio of 1.26, this ratio is 14, an increase of 33%. The implications of

assuming a constant specific heat ratio for the engine flow on vehicle forces and moments are still to be determined, but such large variations within the flowfield and particularly in the vicinity of the nozzle exits will affect the local pressure field, and as such, the structure of the exhaust plumes. Overall heat transfer prediction, including potential ablation and conjugate heat transfer analyses, should include chemistry effects, as the heat transfer on the vehicle is heavily impacted by the engine exhaust. The overall temperature for the chemically-reacting cases considered is much larger than the perfect-gas air condition cases, scaled to permit a single species for the entire solution, investigated previously. While not a focus in this analysis, it should be noted that chemical reactions are also observed about the aft of the vehicle and in the wake downstream, which can potentially impact the vehicle payload.

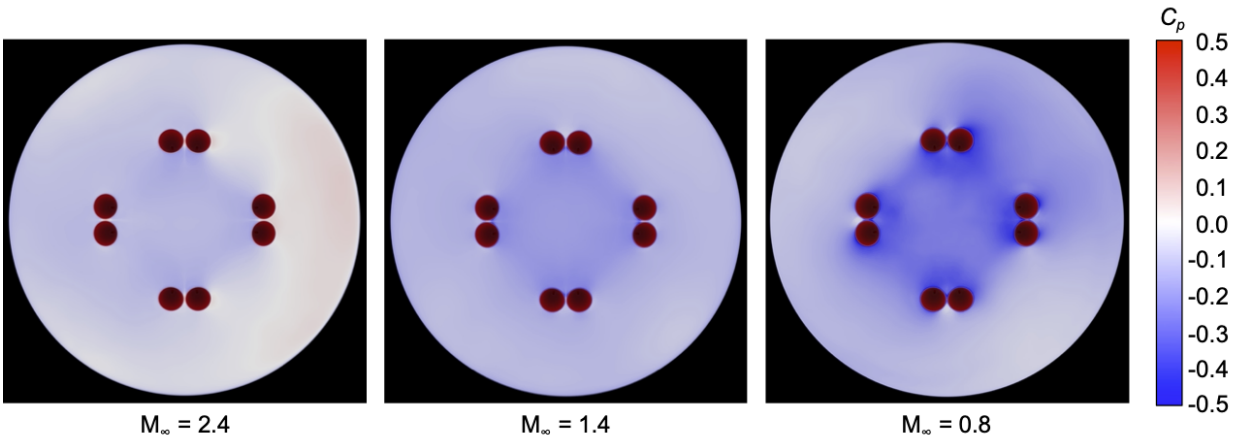

Fig. 23 Heatshield mean C_p distributions for all freestream conditions.

Table 6 Aerodynamic force and moment statistics.

Forebody Aerodynamic Coefficients

	C_A		C_N		$C_{m,ref}$	
Case	μ	σ	μ	σ	μ	σ
Perfect-Gas M_∞ = 2.4	-0.0783	0.0233	0.0134	0.0052	-0.0145	0.0057
Reacting-Gas M_∞ = 2.4	0.0169	0.0310	0.0017	0.0082	-0.0018	0.0092
Reacting-Gas M_∞ = 1.4	-0.1093	0.0344	0.0000	0.0069	-0.0000	0.0075
Reacting-Gas M_∞ = 0.8	-0.1696	0.0606	0.0045	0.0119	-0.0044	0.0115

Total Vehicle Aerodynamic Coefficients

	C_A		C_N		$C_{m,ref}$	
Case	μ	σ	μ	σ	μ	σ
Perfect-Gas M_∞ = 2.4	0.0492	0.0512	0.0122	0.0066	-0.0152	0.0057
Reacting-Gas M_∞ = 2.4	0.1289	0.0333	0.0016	0.0084	-0.0017	0.0091
Reacting-Gas M_∞ = 1.4	0.0368	0.0374	-0.0001	0.0121	0.0000	0.0080
Reacting-Gas M_∞ = 0.8	-0.0805	0.0471	0.0073	0.0202	-0.0049	0.0138

Table 7 Aerodynamic and thrust contributions to total deceleration force.

Case	C_A	$C_{T,x}$	$C_{A,total}$	Aerodynamic Contribution
M_∞ = 2.4	0.1289	2.3305	2.4594	5.241%
M_∞ = 1.4	0.0368	5.0156	5.0524	0.728%
M_∞ = 0.8	-0.0805	13.331	13.251	-0.604%

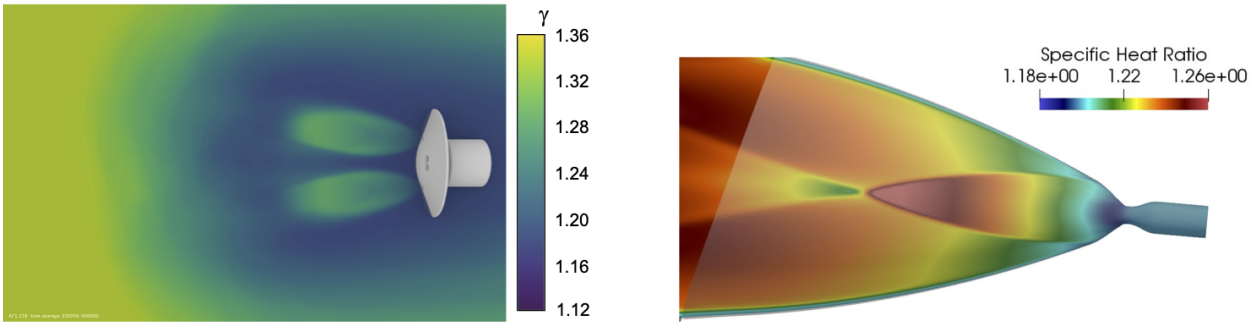

Fig. 24 Mean specific heat ratio contours from Mach 2.4 case (left) and specific heat ratio contours for the internal nozzle flow at 80% throttle (right).

In the absence of validation data beyond subscale, inert gas SRP tests using air as the simulant gases, and no benchmarked CFD solutions, approaches have been applied to reduce approximations simplifications with potential to affect conditions at the nozzle lip. Code-to-code differences for these retropropulsion problems are generally noted between approaches that simulate the full nozzle with a boundary layer and those that interpolate a planar supersonic nozzle inflow profile and in those that lack temperature-dependent thermodynamic properties. The nozzle flow expansion is driven primarily by the pressure differential at the nozzle lip. Any simplifications regarding ignoring or modeling the boundary layer with a wall model should be evaluated against wall-resolved simulations to ensure the simplifications do not lead to different physical phenomena in the external flowfield. Understanding these differences can have impact on the cost of these simulations, as significant expense is required to fully resolve the internal nozzle flows.

V. Summary and Forward Work

Computational fluid dynamics simulations using a GPU-enabled version of the NASA FUN3D flow solver were completed for a conceptual human-scale Mars vehicle at three points along a nominal powered descent trajectory. At each of these conditions (supersonic, transonic, and subsonic), each of the vehicle's eight methane-oxygen engines was throttled to 80%, and a 10-species finite-rate chemistry model was applied to allow full simulation of the Martian atmosphere and engine exhaust during retropropulsion operation. At each condition, significant afterburning was observed external to the nozzles in the large mixing region upstream of the vehicle. Hydroxyl radical mass fractions in excess of 4% were observed throughout the interaction region, along with significant amounts of other species more commonly identified as minor species products for hydrocarbon combustion. Large variations in the specific heat ratio were seen both internal to the nozzle and in the external flowfield. Coupled with significantly increased temperatures over those from prior perfect-gas simulations, the local pressure field is impacted by the variation in composition, the degree of which cannot be fully captured with thermally and chemically frozen flow assumptions. Overall, however, the integrated forces and moments on the vehicle remain small during powered flight, with the aerodynamic contribution to total deceleration force on the vehicle peaking at 5.24% under supersonic conditions.

While there have been numerous experiments for retropropulsion with successful CFD comparisons, including numerous applications of FUN3D, the experiments all involved low-temperature inert gases and simple nozzle configurations. Future experimental data including data to separate composition from chemical reactions through inert gas testing with exhaust flow simulants other than air, hot-fire ground test data, and flight test data for configurations with significant aerodynamic surface area will be necessary for more complete validation and differentiation between computational approaches. Upcoming supersonic wind tunnel testing in the NASA Langley Unitary Plan Wind Tunnel

in early 2022, while still using high-pressure air for the nozzle flow, will test subscale SRP configurations with multiple nozzles, including the 8-nozzle, paired configuration simulated here.

It is the expectation that current and future vehicle designs will be evaluated primarily using CFD methods, with aerodynamics databases for vehicle performance derived from solution approaches and computational tools with a wide range of fidelity in physical modeling. The complexity of including the internal nozzle flows and finite-rate chemistry with a 10-species model was applied in this analysis with an objective to identify regions of the flowfield and integrated vehicle quantities where such complexity may not be required in future applications.

Acknowledgments

This research was sponsored by the NASA Langley Research Center CIF/IRAD program and the NASA Transformational Tools and Technologies (TTT) Project of the Transformative Aeronautics Concepts Program under the Aeronautics Research Mission Directorate. The authors would like to thank the Department of Defense High Performance Computing Modernization Program, NVIDIA, and Sameer Shende of the University of Oregon. This research used resources of the Oak Ridge Leadership Computing Facility at the Oak Ridge National Laboratory, which is supported by the Office of Science of the U.S. Department of Energy under Contract No. DE-AC05-00OR22725.

References

[1] Dwyer Cianciolo, A., and Polsgrove, T., "Human Mars Entry, Descent, and Landing Architecture Study Overview," *AIAA Paper 2016–5494*, 2016.

[2] Dwyer Cianciolo et al, A., "Entry, Descent, and Landing Systems Analysis Study: Phase 1 Report," *NASA Technical Report TM-216720*, 2017.

[3] Dwyer-Cianciolo, A. M., Polsgrove, T., Sostaric, R. R., Edquist, K. T., Korzun, A. M., and Garcia, J. A., "Human Mars Entry, Descent, and Landing Architecture Study: Phase 3 Summary," *AIAA Paper 2020–1509*, 2020. https://doi.org/10.2514/6.2020-1509.

[4] Korzun, A. M., Cruz, J. R., and Braun, R. D., "A Survey of Supersonic Retropropulsion Technology for Mars Entry, Descent, and Landing," *Journal of Spacecraft and Rockets*, Vol. 46, No. 5, 2009, pp. 929–937.

[5] Korzun, A. M., and Cassel, L. A., "Scaling and Similitude in Single Nozzle Supersonic Retropropulsion Aerodynamics Interference," *AIAA Paper 2020–0039*, 2020.

[6] Edquist, K. T., Korzun, A. M., Dyakonov, A. A., Studak, J. W., Kipp, D. M., and Dupzyk, I. C., "Development of Supersonic Retropropulsion for Future Mars Entry, Descent, and Landing Systems," *Journal of Spacecraft and Rockets*, Vol. 51, No. 3, 2014, pp. 650–663. https://doi.org/10.2514/1.A32715.

[7] Trumble, K., "An Initial Assessment of Navier-Stokes Codes Applied to Supersonic Retro-Propulsion," *AIAA Paper 2010–5047*, 2010.

[8] Schauerhamer, D., Trumble, K., Kleb, W., Carlson, J.-R., and Edquist, K., "Continuing Validation of Computational Fluid Dynamics for Supersonic Retropropulsion," *AIAA Paper 2012–864*, 2012.

[9] Kleb, W., Schauerhamer, D., Trumble, K., Sozer, E., Barnhardt, M., Carlson, J.-R., and Edquist, K., "Toward Supersonic Retropropulsion CFD Validation," *AIAA Paper 2011–3490*, 2011.

[10] Edquist, K. T., Korzun, A. M., Bibb, K., Schauerhamer, D. G., Ma, E. C., McCloud, P. L., Palmer, G. E., and Monk, J. D., "Comparison of Navier-Stokes Flow Solvers to Falcon 9 Supersonic Retropropulsion Flight Data," *AIAA Paper 2017–5296*, 2017.

[11] NEcker, T., Zilker, F., Dumont, E., Karl, S., and Hannemann, K., "Aerothermal Analysis of Reusable Launcher Systems During Retro-Propulsion Reentry and Landing," *2018 Space Propulsion Conference Paper 2018–00040*, 2018.

[12] Korzun, A. M., Bibb, K. L., Canabal, F., Childs, R. E., Tang, C. Y., Rizk, Y. M., Van Norman, J. W., and Tynis, J. A., "Powered Descent Aerodynamics for Low and Mid Lift-to-Drag Human Mars Entry, Descent, and Landing Vehicles," *AIAA Paper 2020–1510*, 2020.

[13] Edquist, K. T., Glass, C. E., Korzun, A. M., Wood, W. A., West, T. K., Alter, S. J., Canabal, F., Childs, R. A., Halstrom, L. D., and Matsuno, K. V., "Computational Modeling of Mars Retropropulsion Concepts Tested in the Langley Unitary Plan Wind Tunnel," *To be presented at the 2022 AIAA SciTech Forum*, 2022.

[14] Korzun, A. M., Nielsen, E. J., Walden, A. C., Jones, W. T., Carlson, J.-R., Moran, P. J., Henze, C. E., and Sandstrom, T. A., "Effects of Spatial Resolution on Retropropulsion Aerodynamics in an Atmospheric Environment," *AIAA Paper 2020–1749*, 2020.

[15] Korzun, A., Nielsen, E., Walden, A., Jones, W., Carlson, J.-R., Moran, P., Henze, C., and Sandstrom, T., "Computational Investigation of Retropropulsion Operating Environments with a Massively Parallel Detached Eddy Simulation Approach," *AIAA Paper 2020–4228*, 2020.

[16] Ecker, T., Karl, S., Dumont, E., Stappert, S., and Krause, D., "Numerical Study on the Thermal Loads During a Supersonic Rocket Retropropulsion Maneuver," *Journal of Spacecraft and Rockets*, Vol. 57, No. 1, 2020, pp. 131–146.

[17] Shafner, J. A., and Korzun, A. M., "Computational Analysis of a Multiple-Nozzle Supersonic Retropropulsion Configuration," *AIAA Paper 2021–2556*, 2021.

[18] Nastac, G., Korzun, A., Walden, A., Nielsen, E., Jones, W., and Moran, P., "Computational Investigation of the Effect of Chemistry on Mars Supersonic Retropropulsion Environments," *To be presented at the 2022 AIAA SciTech Forum*, 2022.

[19] Matsuno, K. V., Childs, R. A., Pulliam, T. H., Stremel, P., and Garcia, J. A., "OVERFLOW Analysis of Supersonic Retropropulsion Testing on the CobraMRV Mars Entry Vehicle Concept," *To be presented at the 2022 AIAA SciTech Forum*, 2022.

[20] Halstrom, L. D., Pulliam, T. H., Childs, R. A., and Stremel, P., "OVERFLOW Analysis of Supersonic Retropropulsion Testing on a Blunt Mars Entry Vehicle Concept," *To be presented at the 2022 AIAA SciTech Forum*, 2022.

[21] Jewell, E., and Farhat, C., "Large-Eddy Simulation of Supersonic Retropropulsion Test at NASA Langley Unitary Plan Wind Tunnel," *To be presented at the 2022 AIAA SciTech Forum*, 2022.

[22] Bakhtian, N. M., and Aftosmis, M. J., "Parametric study of peripheral nozzle configurations for supersonic retropropulsion," *Journal of Spacecraft and Rockets*, Vol. 47, No. 6, 2010, pp. 935–950.

[23] ORNL, "Summit," https://www.olcf.ornl.gov/olcf-resources/compute-systems/summit, 2020. Last Accessed November 20, 2020.

[24] Lugo, R. A., Cianciolo, A. M. D., and Powell, R. W., "Overview of a Generalized Numerical Predictor-Corrector Targeting Guidance with Application to Human-Scale Mars Entry, Descent, and Landing," *AIAA Paper 2020–0846*, 2020.

[25] Johnston, C., and Brandis, A., "Modeling of Nonequilibrium CO Fourth-Positive and CN Violet Emission in CO2–N2 Gases," *Journal of Quantitative Spectroscopy and Radiative Transfer*, Vol. 149, 2014, pp. 303–317.

[26] Park, C., Howe, J. T., Jaffe, R. L., and Candler, G. V., "Review of Chemical-Kinetic Problems of Future NASA Missions. II-Mars Entries," *Journal of Thermophysics and Heat transfer*, Vol. 8, No. 1, 1994, pp. 9–23.

[27] Fujita, K., Yamada, T., and Ishii, N., "Impact of Ablation Gas Kinetics on Hyperbolic Entry Radiative Heating," *AIAA Paper 2006-1185*, 2006.

[28] Park, C., *Nonequilibrium Hypersonic Aerothermodynamics*, Wiley, 1989.

[29] Biedron, R. T., Carlson, J. R., Derlaga, J. M., Gnoffo, P. A., Hammond, D. P., Jones, W. T., Kleb, B., Lee-Rausch, E. M., Nielsen, E. J., Park, M. A., et al., "FUN3D Manual: 13.6," *NASA TM-2019-220416*, 2019.

[30] Catris, S., and Aupoix, B., "Density Corrections for Turbulence models," *Aerospace Science and Technology*, Vol. 4, No. 1, 2000, pp. 1–11.

[31] Spalart, P. R., "Comments on the Feasibility of LES for Wings, and on a Hybrid RANS/LES Approach," *Proceedings of First AFOSR International Conference on DNS/LES*, Greyden Press, 1997, pp. 137–147.

[32] Nastac, G., Walden, A., Nielsen, E. J., and Frendi, K., "Implicit Thermochemical Nonequilibrium Flow Simulations on Unstructured Grids using GPUs," *AIAA Paper 2021–0159*, 2021.

[33] Gnoffo, P. A., Gupta, R. N., and Shinn, J. L., "Conservation Equations and Physical Models for Hypersonic Air Flows in Thermal and Chemical Nonequilibrium," *NASA TP 2867*, 1989.

[34] Jones, W. T., "GridEx-An Integrated Grid Generation Package for CFD," *AIAA Paper 2003–4129*, 2003.

[35] Marcum, D., and Gaither, J., "Mixed Element Type Unstructured Grid Generation for Viscous Flow Applications," *AIAA Paper 1999–3252*, 1999.

[36] Biedron, R., and Thomas, J., "Recent Enhancements to the FUN3D Flow Solver for Moving-Mesh Applications," *AIAA Paper 2009–1360*, 2009.

[37] Mehta, M., Canabal, F., Tashakkor, S. B., and Smith, S. D., "Numerical Base Heating Sensitivity Study for a Four-Rocket Engine Core Configuration," *Journal of Spacecraft and Rockets*, Vol. 50, No. 3, 2013, pp. 509–526. https://doi.org/10.2514/1.A32287.

[38] Nastac, G., Tramel, R., and Nielsen, E. J., "Improved Heat Transfer Prediction for High-Speed Flows over Blunt Bodies using Adaptive Mixed-Element Unstructured Grids," *To be presented at the 2022 AIAA SciTech Forum*, 2022.